

# Multielement FSO Transceivers Alignment for Inter-UAV Communications

Asaad Kaadan, *Member, IEEE*, Hazem H. Refai, *Member, IEEE*, and Peter G. LoPresti, *Member, IEEE*

**Abstract**—Given the increased interest in aerial communications, free-space optics (FSO) has gained considerable attention for its ability to deliver wider bandwidth, license-free, and secure communication. FSO was initially developed for fixed platforms. As such, the current push to introduce mobility is one of the greatest challenges for FSO developers. This paper presents the first open-loop alignment/stability analysis of hovering multirotors proven to maintain an FSO link despite inherent instability. Communication distance, wavelength, and platform deviation are among the many parameters evaluated in our model. We characterize fiber-bundle transceivers, as an example of optical arrays and their applicability to aerial FSO communication. Our simulation is based on static lab measurements combined with theoretical analysis and optical geometrical intersection models. Analyses indicated that rotational deviation has a much higher impact on performance than translational deviation. Current commercial multirotor platforms proved adequate for future FSO communication, with 16% to 30% expected throughput when employing suitable optical arrays. We conducted a parametric sweep test to determine optimal and marginal receiver parameters based on platform characteristics and performance metrics. This analysis was conducted and reported as one example of the many applications that our developed mathematical models support.

**Index Terms**—Alignment, deviation, free-space optics (FSO), multi-element, multirotor, optical arrays, UAV.

## I. INTRODUCTION

ACCORDING to a recent study [1], the worldwide Unmanned Aerial Vehicles (UAV) market is projected to double during the next decade from \$5.9 billion annually to \$11.3 billion. As the number of UAV's increases, the demand to network them also increases, requiring the development of a suitable communication system. Free-space Optical (FSO) communication is a good candidate for networking aerial platforms since optical communication blocking is less likely to occur in free space. In addition to high-bandwidth, FSO is license-free, secure, and immune to jamming and interference, which make it well suited for military communications. Notably, FSO links are highly sensitive to transceiver alignment and weather conditions.

Manuscript received June 10, 2014; revised September 19, 2014; accepted October 20, 2014. Date of publication October 24, 2014; date of current version November 19, 2014. This work was supported in part by the NSF Grant NSF-ECCS 1340568 and in part by the Office of the Vice President for Research, University of Oklahoma.

A. Kaadan and H. H. Refai are with the School of Electrical and Computer Engineering, University of Oklahoma, Tulsa, OK 74135 USA (e-mail: asaad.kaadan@ou.edu; hazem@ou.edu).

P. G. LoPresti is with the Department of Electrical Engineering, University of Tulsa, Tulsa, OK 74104 USA (e-mail: peter-lopresti@utulsa.edu).

Color versions of one or more of the figures in this paper are available online at <http://ieeexplore.ieee.org>.

Digital Object Identifier 10.1109/JLT.2014.2364795

Micro UAVs, especially multirotors, constitute an important part of the UAV spectrum, due to their diverse civil and military applications. Establishing FSO communication between multirotors tends to be extremely difficult, and no practical solution, even at short-range communication, is available. Although some high-end systems have been tested for inter-satellite [2], ground-to-space [3]–[6] and ground-to-air [7], [8] optical links, they are typically too heavy and expensive to be used with micro-UAVs. Several solutions have been proposed to overcome FSO strict alignment requirements. Among them is replacing mechanical switching with fast optical switching using fiber bundles combined with optical arrays in [9]–[11]. LEDs, VCSELs, and photo-diodes have been used to construct a multi-transceiver spherical array [12]–[14]. The array-shaped FSO transceivers, whether fiber bundles, LEDs, micro-mirrors, etc., proved promising by offering increased field-of-view and diversity-ready performance [14]–[17].

Alignment and mobility constitute significant challenges for FSO [18]. A number of studies have examined misalignment mitigation [19]–[22], building sway [19], [23], platform vibrations [24], [25], and pointing, acquisition, and tracking (PAT) [14], [26]–[28] for fixed terrestrial FSO links. Some PAT algorithms have also been designed for use in satellite [29], air-to-air (A2A) [30], air-to-ground (A2G) [31] or ground-to-ground [9], [32]–[34] mobile FSO links. However, all studied aerial platforms reported in the literature are either fixed wing aircrafts or high-altitude vehicles that typically experience slow dynamics and require constant motion. To the authors' knowledge, no previous alignment research has been conducted concerning A2A or A2G FSO links using multirotor aircrafts. Multirotors hover in one place and usually encounter rapid dynamic forces and high disturbances. In contrast, high-altitude balloons that can hover in place, are subject to minimal disturbances with slow dynamics.

Building future A2A FSO communication systems, especially among multirotors, requires modeling their unique characteristics, (e.g., flight dynamics, stability, size and power consumption) and the effect each has on communication link performance. In this paper, we present a mathematical model that directly relates multirotors' stability with their mutual alignment. The calculated average percentage alignment (APA) can be used to estimate FSO link availability and throughput, among other important communication metrics.

In Section II part A, we present the mathematical framework to investigate the effect of platform instability on maintaining optical alignment between two multi-rotors. This analysis was introduced in the author's early work published in [35]. The contribution of this paper begins in Section II-C (namely (20)

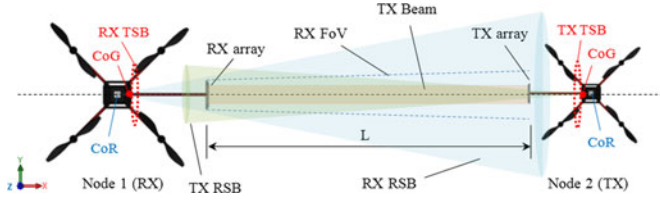


Fig. 1. A typical asymmetric A2A FSO link.

and thereafter). Novel contributions include the generalization of a single optical transmitter design [35] to include multi-fiber/transmitter capable of transmitting with one or multiple fibers. In Section D, an elaborate Beam Angle Index (BAI) parameter is developed to relate power received with the beam incident angle. This relationship is theoretically characterized and verified with lab measurements. In Section III, a computer simulation, with the developed open-loop model, is used to investigate various optical transceiver designs toward combatting instability in aerial platforms. Conclusion remarks, future work, and a summary of contributions are presented in Section IV.

## II. THE A2A FSO ALIGNMENT MODEL

### A. System Description

The aerial nodes and optical transceivers used in this paper are the same as those proposed in our earlier work [35]. Fig. 1 shows a typical asymmetric A2A FSO link where one quadrotor acts as a transmitter and another as a receiver. The alignment model requires only platform output, i.e., Center-of-Gravity (CoG) position and orientation, as an input; thus, the type, size, or hardware/software details of each platform can be neglected. Each quadrotor is deployed separately in a hover state. No spatial or temporal tracking is assumed in this study.

Measured position and orientation data from each aerial node can be fitted with a PDF for each axis with Normal distribution  $N(0, \sigma)$ . After defining translational (linear) and rotational (angular) stability boundaries (TSB and RSB) as  $2\sigma$  and  $4\sigma$  in radius [35], respectively, APA of FSO nodes can then be estimated using the following double-sum:

$$\begin{aligned} \text{APA}(\%) = 100 & \sum_{\substack{y_j, z_j \in \text{RX-TSB} \\ \theta_j, \psi_j \in \text{RX-RSB}}} \sum_{\substack{y_i, z_i \in \text{TX-TSB} \\ \theta_i, \psi_i \in \text{TX-RSB}}} \\ & \cdot P\left(Y_i - \frac{2\sigma_{Y_i}}{y_{\text{grid}}} \leq y_i \leq Y_i + \frac{2\sigma_{Y_i}}{y_{\text{grid}}}\right) \\ & \cdot P\left(Z_i - \frac{2\sigma_{Z_i}}{z_{\text{grid}}} \leq z_i \leq Z_i + \frac{2\sigma_{Z_i}}{z_{\text{grid}}}\right) \\ & \cdot P\left(\Theta_i - \frac{2\sigma_{\Theta_i}}{\theta_{\text{grid}}} \leq \theta_i \leq \Theta_i + \frac{2\sigma_{\Theta_i}}{\theta_{\text{grid}}}\right) \\ & \cdot P\left(\Psi_i - \frac{2\sigma_{\Psi_i}}{\psi_{\text{grid}}} \leq \psi_i \leq \Psi_i + \frac{2\sigma_{\Psi_i}}{\psi_{\text{grid}}}\right) \\ & \cdot P\left(Y_j - \frac{2\sigma_{Y_j}}{y_{\text{grid}}} \leq y_j \leq Y_j + \frac{2\sigma_{Y_j}}{y_{\text{grid}}}\right) \end{aligned}$$



Fig. 2. A 3D representation of a typical aerial communication node (left). Flat and curved optical arrays (right).

$$\begin{aligned} & \cdot P\left(Z_j - \frac{2\sigma_{Z_j}}{z_{\text{grid}}} \leq z_j \leq Z_j + \frac{2\sigma_{Z_j}}{z_{\text{grid}}}\right) \\ & \cdot P\left(\Theta_j - \frac{2\sigma_{\Theta_j}}{\theta_{\text{grid}}} \leq \theta_j \leq \Theta_j + \frac{2\sigma_{\Theta_j}}{\theta_{\text{grid}}}\right) \\ & \cdot P\left(\Psi_j - \frac{2\sigma_{\Psi_j}}{\psi_{\text{grid}}} \leq \psi_j \leq \Psi_j + \frac{2\sigma_{\Psi_j}}{\psi_{\text{grid}}}\right) \\ & \cdot A(Y_i, Z_i, \Theta_i, \Psi_i, Y_j, Z_j, \Theta_j, \Psi_j) \end{aligned} \quad (1)$$

where  $y, z, \theta$  and  $\psi$  represent estimated position and orientation of CoG at a given time epoch; subscript  $i$  denotes the transmitter or UAS 1; and subscript  $j$  denotes the receiver or UAS 2. The *grid* parameter represents quantization step for each axis. The uppercase variables  $Y, Z, \Theta$  and  $\Psi$  are centers of translational and rotational grid segments, i.e., quantized deviation parameters.

The term  $A(Y_i, Z_i, \Theta_i, \Psi_i, Y_j, Z_j, \Theta_j, \Psi_j)$  is called *alignment coefficient*, which describes the alignment between two aerial nodes at a given unique position and orientation combination. The alignment coefficient accepts values between zero and one ( $0 \leq A \leq 1$ ), where  $A = 0$  represents no mutual alignment, and  $A = 1$  represents perfectly aligned platforms. If either node is located outside its own TSB or RSB, the alignment coefficient is set to zero. Alignment coefficients will be calculated using a *geometric intersection* method. Note that translational deviation along the X axis is excluded and can be considered as uncertainty in distance  $L$ . Rotational deviation of roll axis ( $\Phi$ ) is also excluded in this model, given that the optical array is symmetric and centered in the middle of any two motors, i.e., flying at the same altitude (see Fig. 2). LEDs, photodiodes, or fiber bundles can be arranged in a modular fashion to form an optical array as illustrated in Fig. 2. This array is formed either as a flat surface or as a curved one.

### B. Geometric Intersection Models

The mutual alignment of two multi-rotors at a hover state can be modeled by geometrical analysis of transmitter beam(s) intersection with the receiver array at each possible position and orientation combination. Fig. 3 illustrates a typical misalignment configuration with a single transmitter covering the entire transmitter array. CoG is assumed coincident with CoR given the large communication range.

Alignment coefficients are calculated in [35] based on two parameters—beam intersection index (BII):  $f(m_k)$  and

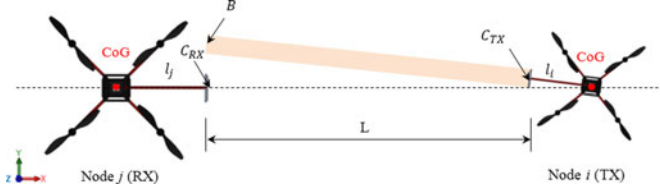


Fig. 3. A typical misalignment configuration.

BAI:  $g(\zeta_k)$ , where:

$$A(Y_i, Z_i, \Theta_i, \Psi_i, Y_j, Z_j, \Theta_j, \Psi_j) = \sum_{k=1}^n \frac{1}{n} f(m_k) g(\zeta_k). \quad (2)$$

Parameter  $n$  represents number of tixel (transmitter-pixel) clusters. Both BAI and BII are calculated based on beam(s) intersection points with the receiver array. The BII provides a percentage of beam footprint intersection with the receiver surface. In single-element receivers, the footprint intersection area does not make such a difference as long as received power exceeds receiver sensitivity level. However, in multi-element receivers, the more rixels (receiver-pixels) the beam covers the better the signal is received and demodulated. Multi-element receivers provide significant enhancements over single element receivers to improve signal quality and combat turbulence and scintillation; they offer the additional capabilities to incorporate and implement spatial and wavelength diversity schemes. The BAI is the beam incident angle normalized to the angle of a perfectly stable beam (normal to receiver surface). Focusing on a single-cluster operation, Eq. (2) can be rewritten as:

$$A(Y_i, Z_i, \Theta_i, \Psi_i, Y_j, Z_j, \Theta_j, \Psi_j) = f(m_k) g(\zeta_k). \quad (3)$$

### C. Flat Transmitter Flat Receiver Model

In the standard case of flat transmitter and flat receiver arrays, the intersection problem can be reduced to solving the intersection between an infinite line (laser beam axis) and an infinite plane coincided with receiver array surface. The entire receiver array surface is assumed light sensitive. In actual design, incident light falling on spaces between receiving elements will not contribute to improving the received signal. Initially, we write infinite plane equations. A three dimensional plane is described using the following equation where constants  $a, b, c$  and  $d$  can be determined using any three different points on that plane:

$$ax + by + cz + d = 0. \quad (4)$$

For simplicity we choose receiver CoG  $(X_0, Y_0, Z_0)$  and two other points. Any translational deviation is added using  $(Y_j, Z_j)$ :

$$P_{RX1} = \begin{bmatrix} X_{RX1} \\ Y_{RX1} \\ Z_{RX1} \\ 1 \end{bmatrix} = \begin{bmatrix} X_0 \\ Y_0 \\ Z_0 \\ 0 \end{bmatrix} + \begin{bmatrix} 0 \\ Y_j \\ Z_j \\ 0 \end{bmatrix}$$

$$P_{RX2} = \begin{bmatrix} X_{RX2} \\ Y_{RX2} \\ Z_{RX2} \\ 1 \end{bmatrix} = \begin{bmatrix} X_{RX1} \\ Y_{RX1} \\ Z_{RX1} \\ 1 \end{bmatrix} + \begin{bmatrix} 0 \\ RA_j \\ 0 \\ 0 \end{bmatrix}$$

$$P_{RX3} = \begin{bmatrix} X_{RX3} \\ Y_{RX3} \\ Z_{RX3} \\ 1 \end{bmatrix} = \begin{bmatrix} X_{RX1} \\ Y_{RX1} \\ Z_{RX1} \\ 1 \end{bmatrix} + \begin{bmatrix} 0 \\ 0 \\ RA_j \\ 0 \end{bmatrix}. \quad (5)$$

$RA_j$  is receiver array radius. These three points are translated and rotated to coincide with receiver array center ( $C_{RX}$ ) and two points on the array circumference:

$$P_1 = C_{RX} = T \times R(\Psi_j) \times R(\Theta_j) \times P_{RX1},$$

$$P_2 = T \times R(\Psi_j) \times R(\Theta_j) \times P_{RX2},$$

$$P_3 = T \times R(\Psi_j) \times R(\Theta_j) \times P_{RX3}. \quad (6)$$

The translation matrix from receiver CoG to receiver array center ( $C_{RX}$ ):

$$T = \begin{bmatrix} 1 & 0 & 0 & l_j \cos \Theta_j \cos \Psi_j \\ 0 & 1 & 0 & l_j \cos \Theta_j \sin \Psi_j \\ 0 & 0 & 1 & l_j \sin \Theta_j \\ 0 & 0 & 0 & 1 \end{bmatrix} \quad (7)$$

where  $l_j$  is the distance between CoG and ( $C_{RX}$ ). Rotation matrices resulting from angular deviation about y-axis (pitch) and z-axis (yaw) are, respectively:

$$R(\Theta_j) = \begin{bmatrix} \cos \Theta_j & 0 & \sin \Theta_j & 0 \\ 0 & 1 & 0 & 0 \\ -\sin \Theta_j & 0 & \cos \Theta_j & 0 \\ 0 & 0 & 0 & 1 \end{bmatrix}$$

$$R(\Psi_j) = \begin{bmatrix} \cos \Psi_j & -\sin \Psi_j & 0 & 0 \\ \sin \Psi_j & \cos \Psi_j & 0 & 0 \\ 0 & 0 & 1 & 0 \\ 0 & 0 & 0 & 1 \end{bmatrix}. \quad (8)$$

Next, we use Cramer's Rule to solve plane equations ( $d = 1$ ) using the three points  $P_1, P_2$  and  $P_3$ :

$$D = \begin{bmatrix} X_1 & Y_1 & Z_1 \\ X_2 & Y_2 & Z_2 \\ X_3 & Y_3 & Z_3 \end{bmatrix}, a = -\frac{d}{D} \begin{bmatrix} 1 & Y_1 & Z_1 \\ 1 & Y_2 & Z_2 \\ 1 & Y_3 & Z_3 \end{bmatrix}$$

$$b = -\frac{d}{D} \begin{bmatrix} X_1 & 1 & Z_1 \\ X_2 & 1 & Z_2 \\ X_3 & 1 & Z_3 \end{bmatrix}, c = -\frac{d}{D} \begin{bmatrix} X_1 & Y_1 & 1 \\ X_2 & Y_2 & 1 \\ X_3 & Y_3 & 1 \end{bmatrix}. \quad (9)$$

The Gaussian laser beam is approximated by a cylinder when beam divergence is ignored or as a cone when divergence is considered. This enables us to use beam axis and footprint radius as an exact representation of the beam itself. A three dimensional line is expressed using the following system of equations:

$$x = x' + ut, \quad y = y' + vt, \quad z = z' + wt. \quad (10)$$

Parameter  $t$  can be chosen arbitrarily.  $(x', y', z')$  is a point on the line. Here, it is the transmitter array center ( $C_{TX}$ ):

$$C_{TX} = \begin{bmatrix} X_{TX} \\ Y_{TX} \\ Z_{TX} \\ 1 \end{bmatrix} = \begin{bmatrix} X_0 \\ Y_0 \\ Z_0 \\ 1 \end{bmatrix} + \begin{bmatrix} L + l_j \\ Y_i \\ Z_i \\ 0 \end{bmatrix}. \quad (11)$$

$u$ ,  $v$  and  $w$  refer to the direction numbers of this line, i.e., the components of any vector  $\vec{M} \langle u, v, w \rangle$  parallel to that line:

$$\begin{aligned} u &= (L + l_i) \cos \theta_i \cos(\psi_i + \pi); \\ v &= (L + l_i) \cos \theta_i \sin(\psi_i + \pi); w = (L + l_i) \sin \theta_i. \end{aligned} \quad (12)$$

$L$  is the communication distance (array to array) and  $l_i$  is distance between CoG and  $C_{TX}$ . Substituting Eq. (12) in Eq. (10) yields a three-dimensional equation describing laser beam axis. Solving equations (10) with equation (4) yields the laser beam axis intersection point with the receiver array plane  $B(x_B, y_B, z_B)$ :

$$\begin{aligned} B_k &= \begin{bmatrix} X_{B_k} \\ Y_{B_k} \\ Z_{B_k} \end{bmatrix} = \begin{bmatrix} X_{TX_k} \\ Y_{TX_k} \\ Z_{TX_k} \end{bmatrix} + \begin{bmatrix} u_k \\ v_k \\ w_k \end{bmatrix} \\ &\times \left( \frac{-a \cdot X_{TX_k} - b \cdot Y_{TX_k} - c \cdot Z_{TX_k} - d}{a \cdot u_k + b \cdot v_k + c \cdot w_k} \right). \end{aligned} \quad (13)$$

We used subscript  $k$  to distinguish laser beams coming from different tixels or different tixel clusters, where:

$B_k$  is the  $k$ th beam intersection point with receiver surface.

$P_{TX_k} = (X_{TX_k}, Y_{TX_k}, Z_{TX_k})$  represents the center of  $k$ th tixel/ $k$ th tixel cluster.

$\vec{M}_k = (u_k, v_k, w_k)$  is the  $k$ th laser beam axis, i.e., the transmitter array normal vector at the  $k$ th tixel/ $k$ th tixel cluster.

In addition to the intersection area calculation, an important factor that contributes to optical signal quality and must be calculated is the incident angle  $\zeta_k$  of  $k$ th beam; it is given by:

$$\zeta_k = \sin^{-1} \left( \frac{|\vec{N}_k \cdot \vec{M}_k|}{|\vec{N}_k| |\vec{M}_k|} \right). \quad (14)$$

$\vec{N}_k$  is the receiver array normal vector at the  $k$ th intersection point, which is parallel to the normal at receiver array center  $C_{RX}$  because the array is flat. Thus, we can write  $\vec{N}_k = \vec{P}_1 \vec{P}_2 \times \vec{P}_1 \vec{P}_3$ . One approach is to calculate the BAI as a linear relationship:

$$g(\zeta_k) = \frac{\zeta_k}{\pi/2}. \quad (15)$$

However, in actual design, it has a nonlinear relationship based on incident angle-power coupling transfer functions. The authors have performed several experiments to characterize the angle-power behavior of their fiber-bundle receiver and transmitter design [36] at three laser wavelengths (e.g., 1550 nm, 1310 nm and 850 nm). More details about incident angle characterization are presented in Section D.

We start with the simplest case where only one tixel at transmitter array center is lit. The intersection area of beam footprint with receiver surface can be calculated by 1) finding the distance between intersection point B and receiver array center  $C_{RX}$ , and 2) finding the intersection of the two circular discs that represent receiver array and transmitter beam footprint, (given that the receiver is a circular disc and the laser beam is Gaussian with a circular footprint).

The distance is given by:

$$\begin{aligned} m &= \|C_{RX} - B\| \\ &= \sqrt{(X_{RX} - X_B)^2 + (Y_{RX} - Y_B)^2 + (Z_{RX} - Z_B)^2}. \end{aligned} \quad (16)$$

Given a laser divergence angle of  $\delta$  radian, the radius of laser beam footprint is given by:

$$r'_i = r_i + L' \cdot \tan \delta \cong r_i + L' \cdot \delta. \quad (17)$$

where  $r_i$  is tixel radius and  $L'$  is the distance between transmitter array center  $C_{TX}$  and intersection point B:

$$\begin{aligned} L' &= \|C_{TX} - B\| \\ &= \sqrt{(X_{TX} - X_B)^2 + (Y_{TX} - Y_B)^2 + (Z_{TX} - Z_B)^2}. \end{aligned} \quad (18)$$

Using equations (16), (17) and receiver array radius  $RA_j$  we determine the BII:

Area  $\pi r^2$  represents maximum intersection area of a single-beam footprint with receiver array surface, where radius  $r$  is the smallest among the two radii, i.e.,  $r = \min(r_i, RA_j)$ . Inserting equations (15) and (19) in equation (3) yields the alignment coefficient for a single-tixel flat transmitter and multi-tixel flat receiver configuration with beam divergence into effect. The lit tixel is located at the center of transmitter array. The general case of a single tixel located anywhere on the transmitter array is calculated by replacing equations (16), (18) and (19) as shown bottom of the page with the following equations, respectively:

$$\begin{aligned} m_k &= \|C_{RX} - B_k\| \\ &= \sqrt{(X_{RX} - X_{B_k})^2 + (Y_{RX} - Y_{B_k})^2 + (Z_{RX} - Z_{B_k})^2} \end{aligned} \quad (20)$$

$$\begin{aligned} L' &= \|P_{TX_k} - B_k\| \\ &= \sqrt{(X_{TX_k} - X_{B_k})^2 + (Y_{TX_k} - Y_{B_k})^2 + (Z_{TX_k} - Z_{B_k})^2} \end{aligned} \quad (21)$$

where  $P_{TX_k}$  is  $k$ th tixel center located anywhere on the array.  $L'$  can still be approximated using equation (18) since distance between the two multi-rotors is much greater than the dimensions of the transmitter and receiver arrays.

In general, a cluster of simultaneously lit tixels is considered; we approximate the cluster of tixels with one tixel transmitting a

$$\begin{aligned} f(m) &= \frac{1}{\pi r^2} \left[ r_i'^2 \cos^{-1} \left( \frac{m^2 + r_i'^2 - RA_j^2}{2mr_i'} \right) + RA_j^2 \cos^{-1} \left( \frac{m^2 + RA_j^2 - r_i'^2}{2mRA_j} \right) \right. \\ &\quad \left. - \frac{1}{2} \sqrt{(-m + r_i' + RA_j)(m + r_i' - RA_j)(m - r_i' + RA_j)(m + r_i' + RA_j)} \right]. \end{aligned} \quad (19)$$



wider and proportional beam. This assumption is made considering that separate beams will ultimately combine forming one beam as they travel over the air due to divergence effect. This is called single-beam approximation. The collimation of beams does not take into account power variations since, in this paper, we are only interested in alignment and coverage. To simplify calculations, we consider the lit tixels pattern to be circular with a radius  $R_i$  and a center located at the  $k$ th tixel. Eq. (16) can be replaced with Eq. (20) and equations (17) through (19) can then be rewritten respectively as:

$$R'_i = R_i + L' \cdot \tan \delta \cong R_i + L' \cdot \delta. \quad (23)$$

$$L' = \|P_{TX_k} - B_k\|$$

$$= \sqrt{(X_{TX_k} - X_B)^2 + (Y_{TX_k} - Y_B)^2 + (Z_{TX_k} - Z_B)^2} \quad (24)$$

Area  $\pi r^2$  is again the maximum intersection area of the transmitter beam footprint with receiver array surface and radius  $r$  is chosen as  $r = \min(R_i, RA_j)$ . Inserting equations (15) and (25) as shown bottom of the page in (3), we determine the alignment coefficient for a multi-tixel flat transmitter and multi-rixel flat receiver configuration with a tixel cluster located anywhere on the transmitter array.

However, the complexity of a transceiver, designed to selectively transmit on one or multiple fibers increases significantly. Furthermore, diversity gain at the receiver, as a consequence of combining multiple channels, is limited by maximum size of the optical transceiver, including photodiodes. Maximum gain is achieved when the minimum distance between two channels guarantees channels are uncorrelated—a condition dependent on turbulence severity. More details about channel correlation for spatial receiver diversity are available in the literature, e.g., [37].

#### D. BAI Characterization

A lab experiment is setup to relate power received and beam incident angle (power-angle). The setup is described in [36] and consists of three transmitting fibers oriented horizontally. Only the center fiber was used. Fig. 4 depicts a schematic for the fiber-bundle transceiver system, and Fig. 6 shows the actual receiver setup with the coupled fibers shown in Fig. 5. Multi and

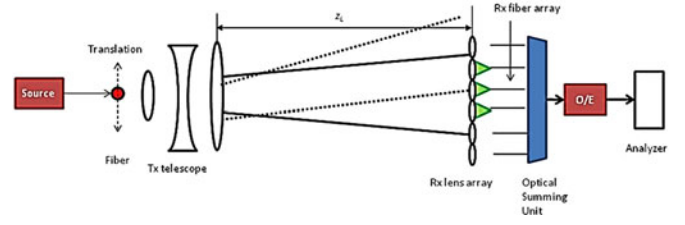


Fig. 4. Fiber bundle transceiver system [38].

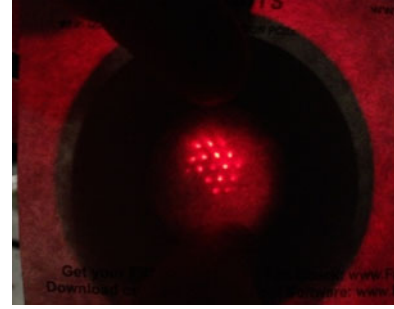


Fig. 5. At the end of the fiber bundle, 15 fibers out of the total 19 are coupled at one configuration [38].

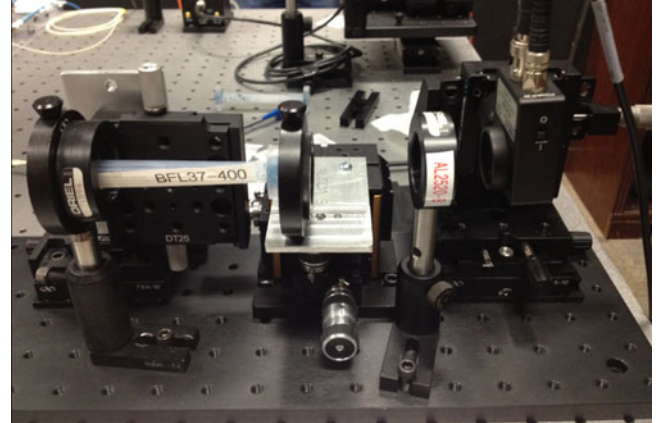


Fig. 6. Coupling fibers at the end of the fiber bundle (Left) and experimental receiver construction (right) [38].

$$f(m_k) = \frac{1}{\pi r^2} \left[ r_i'^2 \cos^{-1} \left( \frac{m_k^2 + r_i'^2 - RA_j^2}{2m_k r_i'} \right) + RA_j^2 \cos^{-1} \left( \frac{m_k^2 + RA_j^2 - r_i'^2}{2m_k RA_j} \right) \right. \\ \left. - \frac{1}{2} \sqrt{(-m_k + r_i' + RA_j)(m_k + r_i' - RA_j)(m_k - r_i' + RA_j)(m_k + r_i' + RA_j)} \right] \quad (22)$$

$$f(m_k) = \frac{1}{\pi r^2} \left[ R_i'^2 \cos^{-1} \left( \frac{m_k^2 + R_i'^2 - RA_j^2}{2m_k R_i'} \right) + RA_j^2 \cos^{-1} \left( \frac{m_k^2 + RA_j^2 - R_i'^2}{2m_k RA_j} \right) \right. \\ \left. - \frac{1}{2} \sqrt{(-m_k + R_i' + RA_j)(m_k + R_i' - RA_j)(m_k - R_i' + RA_j)(m_k + R_i' + RA_j)} \right]. \quad (25)$$

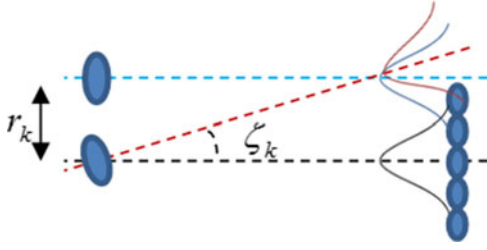


Fig. 7. Rotation and translation of a Gaussian laser beam.

single mode fibers were employed for 850, 1310 and 1550 nm transmitter setup. In each case, the choice of connecting fiber was made in order to maximize the available power from the optical source at the input to the FSO link. Narrative was added in Section II-D in the first paragraph. The two receiving lens arrays were placed on the center axis of the transmitter set-up. The arrays contained plano-convex micro-lenses packed in a hexagonal pattern with a focal length of 3 mm and a diameter of 0.09 in (23 mm) for each lens. An array of nineteen 400  $\mu\text{m}$ -core fibers making up a bundle was located between the two lens arrays with the fibers spaced so that each fiber was behind one of the lenses in the lens array [38].

For power-angle simulation model development, the beam is assumed Gaussian; its waist  $w_L$  at any distance  $z_L$  is [39]:

$$w_L(z_L) = w_{OL} \left( 1 + \left( \frac{\lambda(z_2 + z_L)}{\pi w_{OL}^2} \right)^2 \right)^{\frac{1}{2}}. \quad (26)$$

Solving the equation for  $w_{OL}$  results in:

$$w_{OL} = \frac{\sqrt{2}}{2} \sqrt{w_L^2 - \sqrt{w_L^4 - 4 \frac{\lambda^2(z_2 + z_L)^2}{\pi^2}}}. \quad (27)$$

where  $w_{OL}$  is the beam waist where beam radius of curvature ( $R$ ) is infinite (the beam is collimated),  $\lambda$  is the wavelength and  $z_2 = 40$  mm is the distance between TX fiber and lens.

The intensity distribution at a distance  $z_L$  between the transmitting lens and the receiving lens is given by:

$$I(r) = \frac{2P_t}{\pi w_L^2} \exp(-2r^2/w_L^2) \quad (28)$$

where  $P_t$  is the peak transmission power and  $r$  is the radial distance (translation distance) from the optical axis. Beam divergence can also be calculated using  $w_{OL}$ :

$$\delta = \frac{\lambda}{\pi w_{OL}}. \quad (29)$$

Even though in these experiments the transmitter was not actually rotated (see Fig. 7 in red) but rather translated (see Fig. 7 in blue), we assume small angle rotation will have the same effect on Gaussian beam as translation in order to simplify calculations. Elaborate rotation-based analyses can also be conducted to obtain improved results. The algorithm used to characterize the angle-power relation for the developed fiber-bundle transceiver is described as follows:

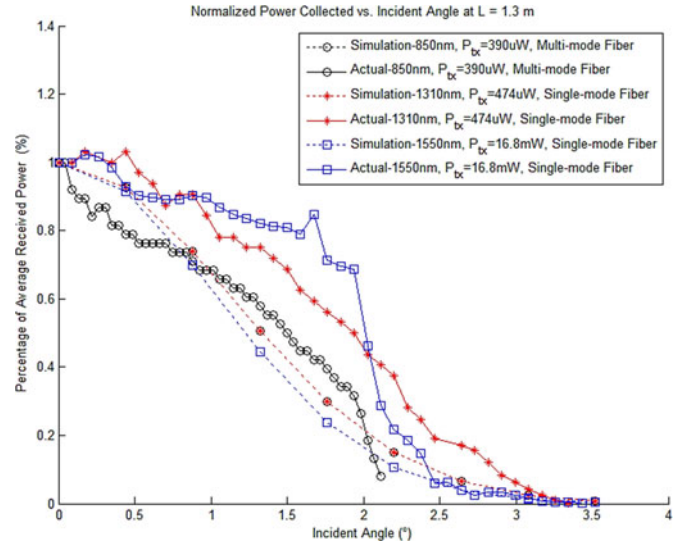


Fig. 8. Normalized received power versus incident angle (measurements and simulation).

- 1) Process lateral deviation-received power measurements at different wavelengths (1550, 1310 and 850 nm) and  $z_L = 1.3$  m to calculate  $w_L(1.3 \text{ m})$  using Eq. 28.
- 2) Use  $w_L(1.3 \text{ m})$  to calculate  $w_{OL}(\lambda)$  (not related to distance) using Eq. 27.
- 3) Calculate  $w_L(z_L, \lambda)$  at any given distance using Eq. 26 and  $w_{OL}$  found in step 2.
- 4) Calculate intensity distribution  $I(r)$  for any transmission power  $P_t$  and lateral deviation  $r$  using Eq. 28 again and  $w_L(z_L)$  from step 3.
- 5) Approximate BAI by the following ratio since lateral deviation is linearly related to the incident angle when the angle is small (see Fig. 7) (The angle is shifted  $90^\circ$ ):

$$g\left(\frac{\pi}{2} - \zeta_k\right) \cong \frac{I(r_k)}{I_0(r_k)} = \exp(-2r_k^2/w_L^2);$$

$$r_k = z_L \tan(\zeta_k) \approx z_L \zeta_k, \quad (30)$$

i.e., BAI is Gaussian distributed in regards to incident angle when the angle is small. Notice that BAI is a function of wavelength and  $w_{OL}$  but not transmission power. Assuming symmetry in both the rixel and the entire receiver array—a valid assumption—enables us to use Eq. 30 to model BAI on both lateral- ( $\psi$ ) and vertical-axis ( $\theta$ ). Normalized received power or intensity, (which can be used as BAI) is shown in Fig. 8 as a function of incident angle and wavelength for measurements and simulations. Disagreement between experimental lab measurements and the simulation model estimations stem from the authors' assumption that the beam is Gaussian. The objective was to prove that the derived model produces a power-angle relationship with a similar tendency and that a good degree of agreement was achieved through experimentation. Obtained simulation results satisfied these conditions. They were also shown to produce conservative power measurements and were bounded by actual experimental results.

TABLE I  
EXTRAPOLATED FIBER-BUNDLE TRANSCIEVER PARAMETERS

	$z_L = L$ (m)	$w_{OL}$ ( $\mu\text{m}$ )	$w_L$ (cm)	$\delta$ (mrad)	BAI (1.5°)
$\lambda = 850 \text{ nm}$	1.3	7.05	5.143	38.38	0.4222
$P_t = 390 \mu\text{W}$	10		38.53		0.3972
	20		76.9		0.3957
$\lambda = 1310 \text{ nm}$	1.3	10.87	5.139	38.35	0.4217
$P_t = 474 \mu\text{W}$	10		38.5		0.3966
	20		76.86		0.3951
$\lambda = 1550 \text{ nm}$	1.3	14	4.72	35.22	0.3617
$P_t = 16.8 \text{ mW}$	10		35.37		0.3343
	20		70.6		0.3327

TABLE II  
ESTIMATED STATISTICAL PARAMETERS FOR ACTUAL MICRO-UAVS  
(MULTIROTORS) [1]

Data Set	Weather	$\sigma_x$ (mm)	$\sigma_y$ (mm)	$\sigma_z$ (mm)
UAS 1 (Hexa)	Light Wind	48	62.6	188.7
UAS 2 (Quad)		62.5	58	258.4
		$\sigma_\varphi$ (°)	$\sigma_\theta$ (°)	$\sigma_\psi$ (°)
UAS 1 (Hexa)		0.337	0.2843	0.1302
UAS 2 (Quad)		0.3138	0.3	0.082
		$\sigma_x$ (mm)	$\sigma_y$ (mm)	$\sigma_z$ (mm)
UAS 1 (Hexa)	Gusty Wind	152.6	202.6	318
UAS 2 (Quad)		324.2	285.4	205.4
		$\sigma_\varphi$ (°)	$\sigma_\theta$ (°)	$\sigma_\psi$ (°)
UAS 1 (Hexa)		1.202	0.9685	0.2262
UAS 2 (Quad)		1.5964	1.9015	0.1977

Another observation is the power-angle relationship overlap for 850 and 1310 nm, primarily because their transmission power is close, as shown in Table I.

### III. SIMULATION AND EXPERIMENTS

#### A. Setup and Results

Multirotor dynamics are hardware-related and rarely analyzed. As such, standard deviation values cannot be gathered from literature. Accordingly, the authors conducted tests on two DIY multirotor platforms (namely a quadrotor and a hexarotor). Onboard-Inertial Measurement Unit, coupled with estimation algorithms, was used to estimate platform dynamics in two weather conditions, as shown in Table II. Resultant numbers provide the base for small-angle approximation, primarily because the maximum measured rotational deviation was 2°. Platforms hovered in place with active stabilization and attitude-control. Hardware details of tested platforms are provided in Table III.

We generated 10 zero-mean Gaussian datasets using various translational and rotational standard deviations (see Table IV). They represent two different multirotors—one used as a transmitter and the other as a receiver. The datasets simulate various levels of platform stability, e.g., very stable, stable, and non-stable platforms. Our experiments on actual state-of-the-art commercial quadrotors and hexarotors yielded deviation num-

TABLE III  
HARDWARE DETAILS OF TESTED MULTIROTORS [40]

Platform	Data Set
Hexarotor, weighed 2.8 kg. Six RCTimer 5010 motors and $15 \times 5.5$ carbon props. Two 6000 mAh, 4 cell batteries. 815 mm motor to motor length. 40 min flight duration.	UAS 1
Quadrotor, weighed 1.8 kg. Four RCTimer 5010 motors and $15 \times 5.5$ carbon props. One 6000 mAh, 4 cell battery. 680 mm motor to motor length. 20 min flight duration.	UAS 2

TABLE IV  
DEVIATION DATA SETS FOR SIMULATED PLATFORMS

#		Translational Deviation (mm)		Angular Deviation (°)		
		<i>TX</i>	<i>RX</i>	<i>TX</i>	<i>RX</i>	
1	$\sigma_y$	0.01	0.01	$\sigma_\theta$	0.01	0.01
	$\sigma_z$	0.01	0.01	$\sigma_\psi$	0.01	0.01
2	$\sigma_y$	15	8	$\sigma_\theta$	0.01	0.01
	$\sigma_z$	12	15	$\sigma_\psi$	0.01	0.01
3	$\sigma_y$	25	18	$\sigma_\theta$	0.3	0.2
	$\sigma_z$	22	35	$\sigma_\psi$	0.8	0.5
4	$\sigma_y$	10	10	$\sigma_\theta$	1	1.2
	$\sigma_z$	11	12	$\sigma_\psi$	0.8	0.9
5	$\sigma_y$	120	150	$\sigma_\theta$	1	1.2
	$\sigma_z$	100	90	$\sigma_\psi$	0.8	0.9
6	$\sigma_y$	0.01	0.01	$\sigma_\theta$	1.5	2
	$\sigma_z$	0.01	0.01	$\sigma_\psi$	2.1	3
7	$\sigma_y$	15	8	$\sigma_\theta$	1.5	2
	$\sigma_z$	12	15	$\sigma_\psi$	2.1	3
8	$\sigma_y$	60	55	$\sigma_\theta$	1.5	2
	$\sigma_z$	80	100	$\sigma_\psi$	2.1	3
9	$\sigma_y$	60	55	$\sigma_\theta$	13	12
	$\sigma_z$	80	100	$\sigma_\psi$	5	7
10	$\sigma_y$	5	3	$\sigma_\theta$	7	5.6
	$\sigma_z$	2	4	$\sigma_\psi$	4.8	6.5

bers similar to dataset 5. We simulated different sets of experiments, labeled from A to G. Each one defines a specific set of hardware and communication parameters, e.g., communication range, beam divergence, array size, transmitter beam pattern, wavelength, transmission power, and others. The algorithm introduced earlier was applied on lab measurements reported in [38] to characterize the BAI and extrapolate other transceiver-related parameters at different communication distances. We present the estimated parameters in Table I. The values in light gray boxes correspond to the same conditions in the actual conducted experiments. As the table shows, the BAI changes with distance are minimal. Thus, we calculate the BAI only once.

Table V lists specific parameters for each experiment. Experiment A demonstrates a single 1 mm tixel pattern at 850 nm. In experiment B, we double the receiver array radius to achieve better performance. Experiment C simulates a shifted single-tixel laser beam located at the circumference of transmitter array. In experiment D, we repeat experiment A with a 1550 nm wavelength laser. Experiment E indicates a multi-tixel single-cluster transmitter with a cluster radius of 60 mm. An all-tixel experiment using the entire transmitter array is conducted in F and G with 10 m and 20 m communication distance, respectively.

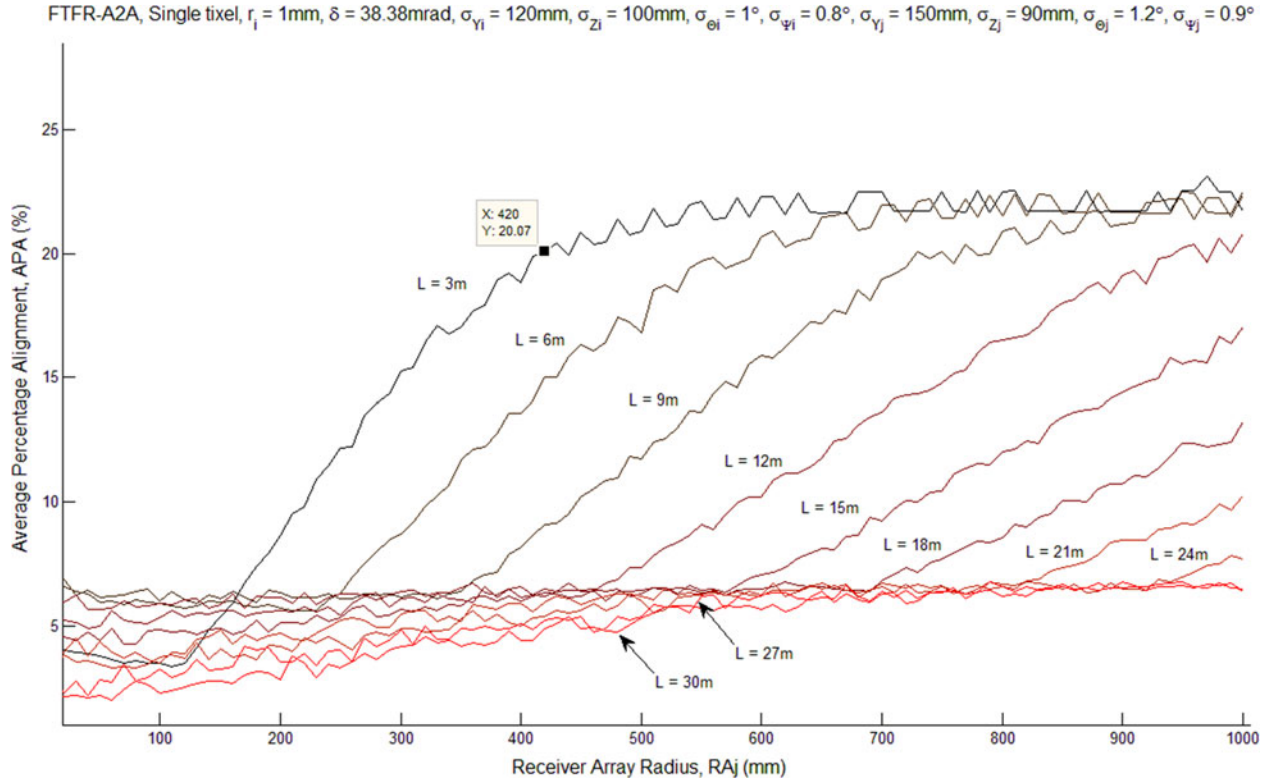


Fig. 9. Parametric sweep for the FTFR A2A model.

TABLE V  
EXPERIMENT PARAMETERS

		Parameters
Common parameters		$r_j = 11.5\text{ mm}$ , $d_j = 23\text{ mm}$ , $i = 250\text{ mm}$ , $l_j = 200\text{ mm}$
A	Single tixel (centered)	$z_L = L = 10\text{ m}$ , $r_i = 1\text{ mm}$ , $RA_j = 230\text{ mm}$ , $P_{TX_k} = (0, 0, 0)$ , $\lambda = 850\text{ nm}$ , $P_t = 390\text{ }\mu\text{W}$
B		$z_L = L = 10\text{ m}$ , $r_i = 1\text{ mm}$ , $RA_j = 460\text{ mm}$ , $P_{TX_k} = (0, 0, 0)$ , $\lambda = 850\text{ nm}$ , $P_t = 390\text{ }\mu\text{W}$
C	Single tixel (shifted)	$z_L = L = 10\text{ m}$ , $r_i = 1\text{ mm}$ , $RA_j = 230\text{ mm}$ , $P_{TX_k} = (0, 150, 150)\text{ mm}$ , $\lambda = 850\text{ nm}$ , $P_t = 390\text{ }\mu\text{W}$
D	Single tixel (centered)	$z_L = L = 10\text{ m}$ , $r_i = 1\text{ mm}$ , $RA_j = 230\text{ mm}$ , $P_{TX_k} = (0, 0, 0)$ , $\lambda = 1550\text{ nm}$ , $P_t = 16.8\text{ mW}$
E	Multi-tixel single-cluster (centered)	$r_{z_L} = L = 10\text{ m}$ , $R_i = 60\text{ mm}$ , $RA_j = 230\text{ mm}$ , $P_{TX_k} = (0, 0, 0)$ , $\lambda = 850\text{ nm}$ , $P_t = 390\text{ }\mu\text{W}$
F	All-tixel	$z_L = L = 10\text{ m}$ , $RA_i = 150\text{ mm}$ , $RA_j = 230\text{ mm}$ , $P_{TX_k} = (0, 0, 0)$ , $\lambda = 850\text{ nm}$ , $P_t = 390\text{ }\mu\text{W}$
G		$z_L = L = 20\text{ m}$ , $RA_i = 150\text{ mm}$ , $RA_j = 230\text{ mm}$ , $P_{TX_k} = (0, 0, 0)$ , $\lambda = 850\text{ nm}$ , $P_t = 390\text{ }\mu\text{W}$

APA results are plotted in Fig. 10. All experimental results match intuitive reasoning and agree with expectations, although some foster interesting observations that will be discussed in the following section. All experiments were conducted using an Intel Core i7-M620 CPU @ 2.67 GHz (4 CPUs), 4 GB of

memory, and Windows 7 (64-bit) platform. All CPU cores were operated in parallel to reduce simulation time. The simulator was written and compiled using MATLAB R2012A (64-bit) environment. Space between stability boundaries was quantized into ten samples per each translational axis and six samples per each rotational axis. The resolution resulted in 12 960 000 alignment coefficients calculated for each experiment and each dataset. The average processing time per experiment per dataset was 3,800 s (i.e., 63 min).

## B. Discussion

Results confirm rotational deviation has a much greater effect on APA than translational deviation. This is clear when comparing datasets 5 and 6 across all experiments. Increasing receiver array radius from 230 mm in A to 460 mm in B has no effect on alignment but almost doubles intersection area. If spatial diversity is employed, SNR is higher and throughput is enhanced. Although performance improvement was high in low rotational deviation datasets (1 through 5), it was minimum with high rotational deviation datasets (6 to 8) and almost absent in very high rotational deviation datasets (9 and 10).

In experiment C, the tixel center was shifted to the circumference of transmitter array, which resulted in 10% less alignment. Experiment D performed worst since the 1550 nm laser has different angle-power characteristics, as easily confirmed by comparing BAI values in Table IV.

Experiments E through F demonstrate the large FoR capability of optical arrays. In E a cluster of tixels with 60 mm radius is lit instead of the 1 mm-tixel, as in previous experiments. Alignment results were improved; however, this was mainly the



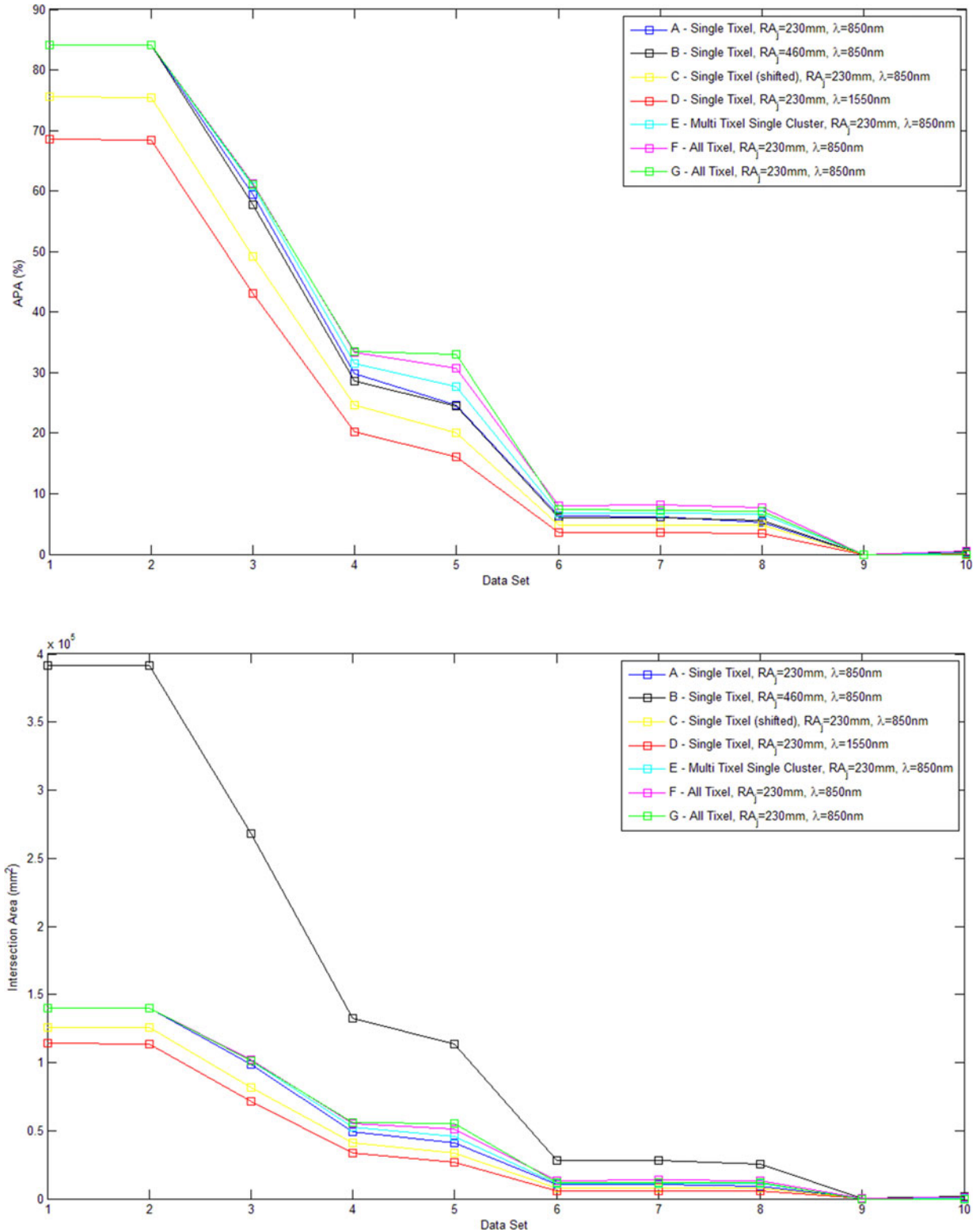


Fig. 10. Simulation Results for Experiments A to G.

case in the low rotational deviation datasets. The same applies to the all-tixel transmission pattern in experiment F. Finally, communication range in experiment G is increased from 10 to 20 m. Performance degradation, compared to experiment F, was high in high-rotational deviation datasets 6, 7 and 8, and otherwise low, primarily because increasing distance magnifies

angular deviation. Hence, performance is greatly reduced regardless of translational deviation. An interesting observation is found in with dataset 5 where increasing the range actually improved alignment performance by at least 15%. This is because increasing distance will increase beam footprint, and as long as received signal power exceeds receiver sensitivity, the increased

beam footprint will compensate for the higher translational deviation experienced in dataset 5.

Highly stable platforms (e.g., datasets 1 and 2) and those with relatively high deviation (e.g., datasets 9 and 10) experienced quantization errors due to space quantization and the 2-sigma stability boundary approximation. These errors are evident in the almost-fixed upper-bound and lower-bound results in all experiments and configurations. The upper-bound numbers only changed when shifting the transmitter from center or adjusting laser wavelength. Increasing space sample points will result in a higher-resolution simulation and more accurate expectations. Experiments B and G show that optical transceiver size is more important than platform stability, or in other words, building a properly designed optical interface could mitigate platform instability. This conclusion is the impetus for developing multi-element transceiver arrays. Having said that, implementing a fully capable multi-element transceiver is extremely complex. Power sharing among multiple fiber increases power loss and reduces the transmission range, thus reducing received optical SNR.

Fig. 9 shows a parametric sweep test for the APA against receiver array radius  $RA_j$  and communication range  $L$ . This graph aids in the design problem where both platform and performance objectives are given; communication system parameters must be designed to meet these objectives. We can determine, for example, the minimum receiver array radius for a given communication range. As shown in the graph, the minimum receiver array radius is 120 mm at a 3 m range (i.e., using an array less than 120 mm in radius will yield less than 5% throughput). If more than 20% mutual alignment is required, then at a 3 m distance, the minimum receiver array radius is 420 mm; at 12 m distance the minimum receiver radius reaches 950 mm. This parametric sweep was conducted for dataset 5, which resembles actual COTS multirotor behavior. To save computation time, resolution was decreased to five samples for each translational axis and to two samples for each rotational axis. The large receiver array size required for achieving acceptable performance indicates the importance of curved optical arrays (or a hybrid array) as alternative solutions to increase FoV/FoR without sacrificing size, weight, and power (SWAP) requirements. Future research will investigate spherical receiver/transmitter arrays to increase FoV/FoR in open loop, non-tracking implementations. Alternatively, incorporating closed loop feedback systems with optical tracking for unstable platforms will greatly enhance performance (i.e., reduce required array size in flat and curved configurations).

#### IV. CONCLUSION

A novel alignment model and simulator for A2A FSO links was presented in this paper. Effects of multirotor instability on communication link availability and performance were analyzed and modeled for the first time in literature. A modeling framework was designed to support multi-element optical transceiver arrays with various parameters that could be analyzed and tuned (e.g., array size, communication range, beam divergence, beam wavelength, platform dynamics, and others).

The APA was calculated as an indication of FSO link availability due to platform deviation. Power/angle behavior of a fiber-bundle based transceiver was measured and characterized across different wavelengths and transmission ranges. The alignment model was tested with several simulated multirotors. Notably, simulation analysis indicated that current state-of-the-art commercial multirotors are ready for A2A FSO implementations given a suitable optical array. Simulation platforms that mimic actual multirotor behavior demonstrated 16% to 30% mutual alignment over a short distance.

This study is also the first to combine stability analysis of multirotors with power analysis of fiber-bundle FSO transceivers in anticipation of combining these two technologies as a suggested solution for future mobile FSO communication. Admittedly, the implementation of a short-distance FSO link between two hovering multirotors would have been tremendously useful for assessing our analysis. However, at the time of this publication, there was unfortunately no FSO technology sufficiently small, lightweight, and agile to the extent that it could be positioned aboard small UAVs. The study presented herein aims to provide a systematic way to characterize platform instability effects on FSO links and demonstrate advantages of open-loop optical array designs. The analyses developed can be incorporated into future closed loop systems and enhance tracking, alignment prediction, and immunity to disturbance. Future development will be directed in two paths. First, we will extend the simulator with curved transceiver arrays, laser-beam propagation models, and multi-cluster transmission patterns. Second, we will continue to build small, lightweight, and large FoV/FoR FSO technology including our fiber-bundle transceiver and other multi-element FSO arrays.

#### REFERENCES

- [1] A. Kaadan, "A Study of Unmanned Aerial Systems Stability for Lasercom Applications," MSc., Elect. Comput. Eng., Univ. Oklahoma, 2013.
- [2] J. E. Mulholland and S. A. Cadogan, "Intersatellite laser crosslinks," *IEEE Trans. Aerospace Electron. Syst.*, vol. 32, no. 3, pp. 1011–1020, Jul. 1996.
- [3] M. Reyes Garcia-Talavera, A. Alonso, S. Chueca, J. J. Fuensalida, Z. Sodnik, V. Cessa *et al.*, "Ground to space optical communication characterization," *Proc. SPIE*, vol. 5892, 2005.
- [4] T. Morio, T. Kenichi, K. Toshiaki, K. Werner, T. Masahiro, K. Hiroo *et al.*, "Results of ground-to-space optical communications experiments using a low earth orbit satellite," in *Proc. IEEE 19th Annu. Meeting Lasers Electro-Opt. Soc.*, 2006, pp. 80–81.
- [5] K. E. Wilson, J. Kovalik, A. Biswas, M. Wright, W. T. Roberts, Y. Takayama *et al.*, "Preliminary results of the OCTL to OICETS optical link experiment (OTOOLE)," *Proc. SPIE*, vol. 7587, pp. 758703–758703, 2010.
- [6] K. E. Wilson, J. R. Lesh, K. Araki, and Y. Arimoto, "Overview of the ground-to-orbit lasercom demonstration (GOLD)," *J. Space Commun.*, vol. 15, pp. 89–95, 1998.
- [7] J. Cunningham, D. Foulke, T. Goode, D. Baber, B. Gaughan, M. Fletcher, D. W. Young, J. C. Juarez, J. E. Sluz, J. L. Riggins, "Long range field testing of free space optical communications terminals on mobile platforms," in *Proc. IEEE Mil. Commun. Conf.*, 2009, pp. 1–7.
- [8] F. G. Walther, G. A. Nowak, S. Michael, R. Parenti, J. Roth, J. Taylor *et al.*, "Air-to-ground lasercom system demonstration," in *Proc. Mil. Commun. Conf.*, 2010, pp. 1594–1600.
- [9] D. Zhou, P. G. LoPresti, and H. H. Refai, "Evaluation of fiber-bundle based transmitter configurations with alignment control algorithm for mobile FSO nodes," *J. Lightw. Technol.*, vol. 31, no. 2, pp. 249–256, Jan. 2013.
- [10] D. Zhou, P. G. LoPresti, and H. H. Refai, "Enlargement of beam coverage in FSO mobile network," *J. Lightw. Technol.*, vol. 29, no. 10, pp. 1583–1589, May 2011.

- [11] K. H. Heng, W.-D. Zhong, and T. H. Cheng, "Multipoint free-space optics system for short-range communications between flight platforms," *Appl. Opt.*, vol. 49, pp. 258–266, Jan. 10, 2010.
- [12] B. Nakhkoob, M. Bilgi, M. Yuksel, and M. Hella, "Multi-transceiver optical wireless spherical structures for MANETs," *IEEE J. Select. Areas Commun.*, vol. 27, no. 9, pp. 1612–1622, Dec. 2009.
- [13] M. Yuksel, J. Akella, S. Kalyanaraman, and P. Dutta, "Free-space-optical mobile ad hoc networks: Auto-configurable building blocks," *Wireless Netw.*, vol. 15, pp. 295–312, Apr. 01, 2009.
- [14] A. Sevincer, M. Bilgi, and M. Yuksel, "Automatic realignment with electronic steering of free-space-optical transceivers in MANETs: A proof-of-concept prototype," *Ad Hoc Netw.*, vol. 11, pp. 585–595, 2013.
- [15] H. Moradi, H. H. Refai, and P. G. LoPresti, "Circular MIMO FSO nodes with transmit selection and receive generalized selection diversity," *IEEE Trans. Veh. Technol.*, vol. 61, no. 3, pp. 1174–1181, Mar. 2012.
- [16] H. Moradi, H. H. Refai, and P. G. LoPresti, "Spatial diversity for fiber-bundled FSO nodes with limited mobility," *J. Lightw. Technol.*, vol. 30, no. 1, pp. 175–183, Jan. 2012.
- [17] M. Bilgi, "Multi-transceiver free-space-optical structures for mobile Ad-Hoc networks," Ph.D. dissertation, Dept. Comput. Sci. Eng., University of Nevada, Reno, NV, USA, 2010.
- [18] S. Bloom, E. Korevaar, J. Schuster, and H. Willebrand, "Understanding the performance of free-space optics [Invited]," *J. Opt. Netw.*, vol. 2, pp. 178–200, 2003.
- [19] H. G. Sandalidis, "Optimization models for misalignment fading mitigation in optical wireless links," *IEEE. Commun. Lett.*, vol. 12, no. 5, pp. 395–397, May 2008.
- [20] A. A. Farid and S. Hranilovic, "Outage capacity for MISO intensity-modulated free-space optical links with misalignment," *IEEE/OSA J. Opt. Commun. Netw.*, vol. 3, no. 10, pp. 780–789, Oct. 2011.
- [21] A. García-Zambrana, C. Castillo-Vázquez, and B. Castillo-Vázquez, "Outage performance of MIMO FSO links over strong turbulence and misalignment fading channels," *Opt. Exp.*, vol. 19, pp. 13480–13496, 2011.
- [22] A. Harris, J. J. J. Sluss, H. H. Refai, and P. G. LoPresti, "Analysis of beam steering tolerances and divergence for various long range FSO communication links," *Proc. SPIE*, vol. 5819, pp. 455–462, 2005.
- [23] X. Liu, "Free-space optics optimization models for building sway and atmospheric interference using variable wavelength," *IEEE Trans. Comm.*, vol. 57, no. 2, pp. 492–498, Feb. 2009.
- [24] A. Harris, J. J. J. Sluss, H. H. Refai, and P. G. LoPresti, "Comparison of active beam steering elements and analysis of platform vibrations for various long-range FSO links," *Proc. SPIE*, vol. 5819, pp. 474–484, 2005.
- [25] B. G. Bonev, "Influence of random fluctuations of laser beam propagation direction on FSO power design," in *Proc. IEEE. Conf. Microw. Tech.*, 2013, pp. 95–100.
- [26] T.-H. Ho, S. D. Milner, and C. C. Davis, "Fully optical real-time pointing, acquisition, and tracking system for free space optical link," *Proc. SPIE*, vol. 5712, pp. 81–92, 2005.
- [27] G. A. Cap, H. H. Refai, and J. J. Sluss, "Optical tracking and auto-alignment transceiver system," *IEEE Aerosp. Electron. Syst. Mag.*, vol. 25, no. 9, pp. 26–34, Sep. 2010.
- [28] T.-H. Ho, "Pointing, acquisition, and tracking systems for free-space optical communication links," Ph.D. Dissertation, Dept. Elect. Eng., Univ. Maryland, College Park, MD, USA, 2007.
- [29] M. Guelman, A. Kogan, A. Kazarian, A. Livne, M. Orenstein, and H. Michalik, "Acquisition and pointing control for inter-satellite laser communications," *IEEE Trans. Aerosp. Electron. Syst.*, vol. 40, no. 4, pp. 1239–1248, Oct. 2004.
- [30] S. S. Muhammad, T. Plank, E. Leitgeb, A. Friedl, K. Zetl, T. Javornik *et al.*, "Challenges in establishing free space optical communications between flying vehicles," in *Proc. 6th Int. Symp. Commun. Syst., Netw. Digital Signal Process.*, 2008, pp. 82–86.
- [31] A. Harris, J. J. Sluss, H. H. Refai, and P. G. LoPresti, "Alignment and tracking of a free-space optical communications link to a UAV," in *Proc. 24th Digital Avionics Syst. Conf.*, 2005, vol. 1, pp. 1.C.2–1.1–9.
- [32] R. Paudel, Z. Ghassemlooy, L.-M. Hoa, S. Rajbhandari, and B. Livingstone, "Investigation of FSO ground-to-train communications in a laboratory environment," in *Proc. 2nd Asian Himalayas Int. Conf. Internet*, 2011, pp. 1–5.
- [33] D. Zhou, H. H. Refai, P. G. LoPresti, and M. Atiquzzaman, "Control algorithm development for mobile FSO node alignment," in *Proc. IEEE/AIAA 28th Digital Avionics Syst. Conf.*, 2009, pp. 6.A.3–1–6.A.3–12.
- [34] R. Paudel, Z. Ghassemlooy, L.-M. Hoa, and S. Rajbhandari, "Modelling of free space optical link for ground-to-train communications using a Gaussian source," *IET Optoelectronics*, vol. 7, pp. 1–8, 2013.
- [35] A. Kaadan, D. Zhou, H. H. Refai, and P. G. LoPresti, "Modeling of aerial-to-aerial short-distance free-space optical links," in *Proc. Integr. Commun., Navigat. Surveillance Conf.*, 2013, pp. 1–12.
- [36] P. G. LoPresti, W. Yi, E. Rohlman, and H. Refai, "Wavelength diversity assessment of fiber bundle receiver under misalignment and turbulence," *Proc. SPIE*, vol. 8732, pp. 87320C-1–87320C-8, 2013.
- [37] C. Zhixiao, Y. Song, W. Tianyi, W. Guohua, W. Shaoling, and G. Wanyi, "Channel correlation in aperture receiver diversity systems for free-space optical communication," *J. Opt.*, vol. 14, p. 125710, 2012.
- [38] W. Yi, "Experimental evaluation of wavelength diversity based on fiber-bundle receiver design," Master Thesis, Dept. Elect. Eng., University Tulsa, Tulsa, OK, USA, 2013.
- [39] P. LoPresti, H. Refai, J. Sluss, and I. Varela-Cuadrado, "Adaptive divergence and power for improving connectivity in free-space optical mobile networks," *Appl. Opt.*, vol. 45, pp. 6591–6597, Sep. 01, 2006.
- [40] A. Kaadan, "A study of unmanned aerial systems stability for laser-com applications," Master Thesis, Dept. Sci., Elect. Comput. Eng., Univ. Oklahoma, Tulsa, OK, USA, 2013.

**Asaad Kaadan (M'11)** received the B.S. degree (first rank Hons.) in electronics engineering from Aleppo University, Aleppo, Syria, in 2010, with and the M.Sc. degree in electrical and computer engineering from the University of Oklahoma, Tulsa, OK, USA, in 2013 with 4.0 GPA. He is currently working toward the Ph.D. degree with the Electrical and Computer Engineering Department, the University of Oklahoma. His research interests include control theory, embedded systems, robotics, unmanned aerial systems, wireless sensor networks, security and mobile free-space optics. He received an Honorable Mention on his paper at ICNS 2013 conference and a Best Paper Award at IWCNC 2013 conference.

**Hazem H. Refai (M'99)** received the M.S.E.E. and Ph.D. degrees from the University of Oklahoma (OU), Norman, OK, USA, in 1993 and 1999, respectively. He currently serves as an Associate Professor with the Department of Electrical and Computer Engineering Telecommunication Program in Tulsa, OU. He is the Founder and Director of OU's Wireless Electromagnetic Compliance and Design Center, where he and his team focus on basic and applied research in radio-frequency and optical wireless communication and networks, as well as electromagnetic compatibility. His research interests include the development of physical and medium-access control layers for mobile laser communication networks using free space optics, cognitive radios and networks, sensor-based autocollision avoidance systems, vehicle-to-vehicle communication protocols, and portable hybrid RF/free-space-optical communication systems for disaster recovery.

**Peter G. LoPresti (M'94)** received the B.S.E. degree in electrical engineering from the University of Delaware, Newark, DE, USA, in 1988, and the Ph.D. degree in electrical engineering from The Pennsylvania State University, University Park, PA, USA, in 1994. He currently serves as a Professor of electrical engineering with the University of Tulsa, Tulsa, OK, USA. He is the Director of the Williams Communications Optical Networking Laboratory, Department of Electrical Engineering, University of Tulsa, and a Project Consultant for a company developing 3-D displays. His research interests include optical communication systems engineering; mobile free-space optical communication network design and implementation for disaster recovery, environmental monitoring, and battlefield communication; and optical sensor development for environmental monitoring.